Z. Phys. Chem. **223** (2009) 1047–1062 / **DOI** 10.1524/zpch.2009.6057

Molecular Dynamics Simulations on the Glass-to-liquid Transition in High Density Amorphous Ice

By Markus Seidl[1,2], Thomas Loerting[2,*], and Gerhard Zifferer[1,**]

[1] Department of Physical Chemistry, University of Vienna, Währinger Str. 42, A-1090 Vienna, Austria
[2] Institute of Physical Chemistry, University of Innsbruck, Innrain 52a, A-6020 Innsbruck, Austria

Dedicated to Prof. Dr. Alfons Geiger on the occasion of his 65th birthday

(Received May 15, 2009; accepted May 29, 2009)

Glass-to-liquid Transition / High Density Amorphous Ice / Molecular Dynamics Simulations / Water

It is an open question whether high density amorphous (HDA) ice is a glassy material structurally related to an ultraviscous high density liquid (HDL) or a nanocrystalline material unrelated to a liquid. In order to shed light on this question we have performed molecular dynamics simulations on a HDA model system at a pressure of $p \approx 0.3$ GPa using the COMPASS force field. After removing the irreversible structural relaxation effect by initial isobaric heating/cooling cycles, we observe a deviation from linearity in the density vs. temperature plot in the range 170 ± 15 K in subsequent cycles, which we attribute to the glass-transition temperature T_g. This assignment of T_g is corroborated by two independent methods, namely from a rapid increase in the diffusion coefficient at ≈169 K and a deviation from linearity at ≈174 K in an enthalpy versus temperature plot. The structure of the model system is in good agreement with the experimentally determined structure of HDA. We, thus, suggest that HDA may indeed be a low temperature structural proxy of an ultraviscous liquid HDL.

1. Introduction

Even though the phase-diagram of water and the metastable states not in the phase-diagram have been the subject to intense research for more than 100 years, there are still many questions unresolved [1–3]. New (metastable) crystalline

* Corresponding author. E-mail: thomas.loerting@uibk.ac.at
** Corresponding author. E-mail: gerhard.zifferer@univie.ac.at

phases such as ice XII [4], XIII and XIV [5] were discovered in the last decade, and it is known that some proton-ordered ice phases at moderate pressures and some phases at extremely high pressures ("post-ice X phases") await their experimental confirmation. In this article we focus on questions related to the phase-diagram of non-crystalline states of water at low temperatures, which is depicted schematically in Fig. 1 up to 0.35 GPa. A liquid metastable with respect to the crystalline solid can be prepared by cooling water below its melting point T_M, which is denoted "supercooled water". Below the homogeneous nucleation line T_H water crystallizes very quickly, and so the supercooled liquid can not be studied in the "No man's land" at $T < T_H$ [6]. There are ways of preparing non-crystalline water at $T << T_H$, though. At least five methods have been used to make amorphous (non-crystalline) ice [7–14]. Despite of the many ways of preparing amorphous ices, they can be categorized into three distinct structural states, namely low- (LDA), high- (HDA) and very high density amorphous ice (VHDA) [15]. Upon heating the LDA structural state to beyond $T_g \approx 136$ K at 1 bar the structural relaxation dynamics changes from the one typical for a glassy solid to the one typical for a (deeply) supercooled liquid, which is called low density liquid (LDL) [16, 17]. This transition is called a glass-to-liquid transition, which is (by contrast to, e.g., the melting transition of ice) not a phase transition in the strict thermodynamic sense, but affected by the thermal history of the glass and kinetic effects, e.g., when varying heating/cooling rates. On continued heating LDL crystallizes at $T_X \approx 150$ K (1 bar), and therefore the question whether LDL is continuously connected with the supercooled liquid at $T > T_H \approx 231$ K (1bar) is debated. In order to discriminate LDL at $T < T_X$ from the supercooled liquid at $T > T_H$, it is denoted "deeply supercooled". It is still unresolved whether there are also deeply supercooled liquids emanating on heating HDA (and also VHDA), which is indicated by the "?" in Fig. 1. While high-pressure dielectric relaxation studies [18, 19] and high-pressure vitrification studies [20] suggest the existence of the deeply supercooled high density liquid (HDL), other studies suggest HDA to be a nanocrystalline material unrelated to a deeply supercooled liquid [21–23].

Computational methods have proven over the last few decades that they are a versatile tool for complementing experimental results and performing analyses, where the experiment has limitations. In particular, the phase diagram of both crystalline and disordered forms of water was the focus of many studies employing a wide range of force fields [24–32]. Questions such as the possibility of liquid-liquid phase segregation and the possible occurrence of a liquid-liquid critical point have been addressed at the nanosecond time scale in the absence of crystallization effects [33–43], where experimentally rapid crystallization takes place ("no-man's land"). Success and limitations of such numerical simulations have recently been reviewed [3].

In order to shed light on the question whether HDA is a low-temperature proxy to HDL we here perform molecular dynamics simulations on the glass-to-liquid transition. Starting with an amorphous model systems of water at a density

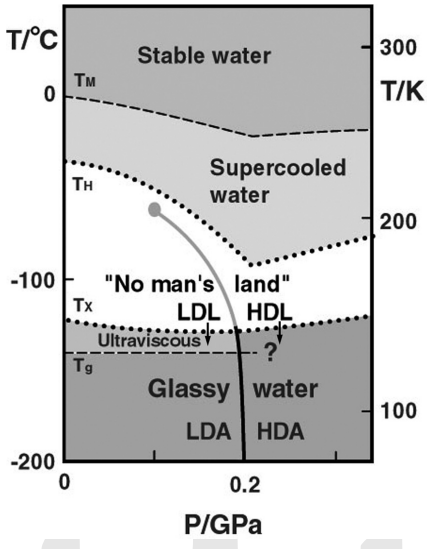

Fig. 1. "Phase" diagram of non-crystalline water showing stable and metastable states. TM… melting temperature, TH…homogeneous nucleation temperature, TX…crystallization temperature, Tg…glass-to-liquid transition temperature, LDA…low density amorphous ice, HDA… high density amorphous ice, LDL…ultraviscous low density liquid, HDL…ultraviscous high density liquid. Adapted from Mishima&Stanley, Phys. Chem. Chem. Phys. **2** (2000) 1551–1558.

corresponding to HDA at low temperatures several heating and cooling runs are simulated at a pressure of 0.3 GPa in order to determine T_g. There are many ways of monitoring a glass-to-liquid transition [44], e.g., by monitoring the stepwise increase in heat capacity c_p in differential scanning calorimetry experiments or by monitoring the stepwise change in expansivity β in dilatometry experiments, which corresponds to a kink in the density vs. temperature curve [45]. In the current investigation we use the latter one, based on our experience with the determination of glass transition temperatures of polymers [46, 47] and carbohydrates [48] by means of isothermal-isobaric molecular dynamics simulations. In addition, corroborating information was obtained from enthalpy versus T curves and the behaviour of the diffusion coefficient. By contrast to experiments, at the ultrahigh heating rates employed in simulations crystallization does not interfere in the vicinity of T_g. While some simulation work has been devoted to studying the glass-to-liquid transition in LDA [49, 50], we are not aware of any literature study analyzing the possibility of a glass-to-liquid transition in HDA or VHDA.

2. Model and methods

The molecular dynamics simulations were performed by use of Materials Studio® (3.0, 4.4) from Accelrys Inc.:

First, by use of the *Amorphous Cell* tool a cubic box (with periodic boundaries in all directions) containing $N = 512$ water molecules was prepared at a density of 1.16 g/cm^3 (box length ≈ 2.36 nm) characteristic of HDA at 1 bar [10]. In this step the box was filled with non-overlapping water molecules followed by a small energy minimization run to remove energetically unfavorable configurations. Second, a molecular dynamics run at constant volume and temperature (NVT) was performed for a period of 1 ns at a temperature $T = 70$ K monitoring the actual pressure of the system which was 0.32 GPa on average, see left column of Fig. 2. Third, starting with the last frame of the NVT run a constant temperature and constant pressure molecular dynamics simulation (NPT) at $T = 70$ K and $p = 0.3$ GPa allowed the system to adjust the volume and density according to the simulation parameters (see right column of Fig. 2), the pressure being chosen according to the results of the NVT run. As the whole process occurred at the very low temperature 70 K the initial configuration obtained in this way should correspond to unrelaxed HDA, termed u-HDA [3, 51].

In order to allow for relaxation and to simulate the density ρ versus temperature T curve (which in turn yields the basis for the determination of T_g), the system was heated in steps of 10 K until a maximum temperature (160 K in the first, 200 K in the second, and 220 K in further cycles) was reached. Afterwards, a cooling process was initiated by lowering the temperature in steps of 10 K until the lowest temperature (70 K) was reached. Then, the cycle was started again. At each temperature a 500 ps run was performed – 250 ps for equilibration and 250 ps for data sampling (i.e. averaging the density ρ as well as the actual temperature and pressure) using the final configuration of a run as the starting structure for the next temperature (10 K higher and lower, respectively). As an example a part of a typical heating run is depicted in Fig. 3, showing the temperature program as well as the density as a function of simulation time.

Module *Discover* was the molecular dynamics engine (using the Andersen thermostat and barostat [52] with a time step of 1 fs applying the Verlet velocity algorithm [53]) making use of the force field COMPASS. A cut-off distance of 1.25 nm with a spline switching function (0.3 nm width) was applied for the nonbonding interactions (i.e., for Coulomb and for van der Waals interactions, the latter one being expressed by a 9–6 Lennard-Jones potential). Furthermore, charge groups were used to prevent dipoles from being artificially split when one of the atoms was inside and another was outside the atom-based cut-off. Clearly, also in cases where the cut-off distance exceeded half of the box-length only the nearest of all periodic images was taken into consideration due to the minimum image box convention.

The force field COMPASS is optimized for the simulation of condensed phases, see refs. [54–59] for parameterization and validation and ref. [60] for

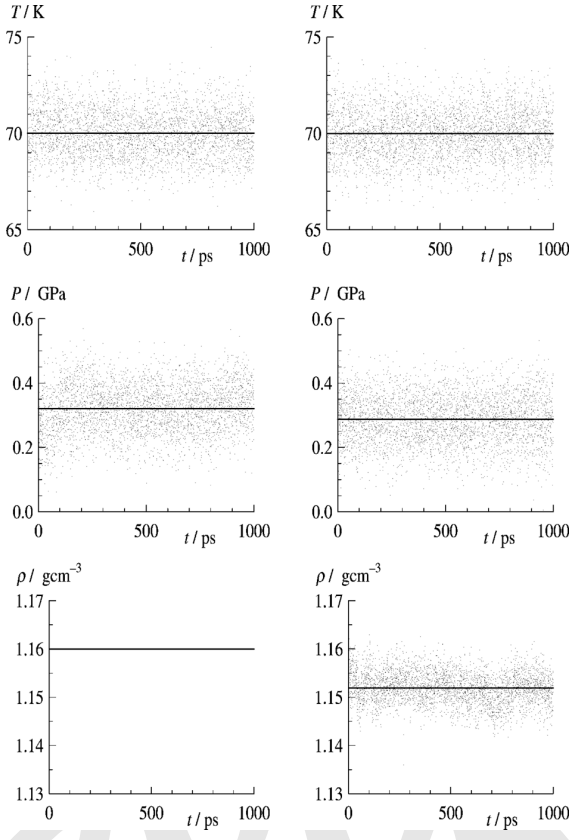

Fig. 2. Time evolution of temperature (top), pressure (middle) and density (bottom) within an MD run at constant volume and temperature (left column) and an MD run at constant pressure and temperature (right column).

fluid density predictions including water. The water model incorporated in COMPASS is a simple three-point model. The (unperturbed) bond length l_0 = 0.0957 nm and bond angle θ_0 = 104.52° as well as the atom charges q_O = −0.82e and q_H = +0.41e are similar to the TIP3P model. However, bond length l and angles θ are not rigid in COMPASS, but modeled as sums of harmonic terms $k_n(l - l_o)^n$ or $k_n(\theta - \theta_o)^n$, respectively, with n = 2,3,4, further including bond-bond and bond-angles cross terms. Force field parameters were parameterized in order to work close to ambient conditions and below [60].

In addition, preliminary investigations were carried out with modified versions of the TIP3P [61] and SPC/E [62] force field, termed TIP3P* and SPC/E*, respectively. Contrary to rigid molecules in the original version, flexible molecules are defined with harmonic bond and angle potentials (quadratic terms only and no cross terms) using the bond and angle parameters of TIP3P and SPC/E,

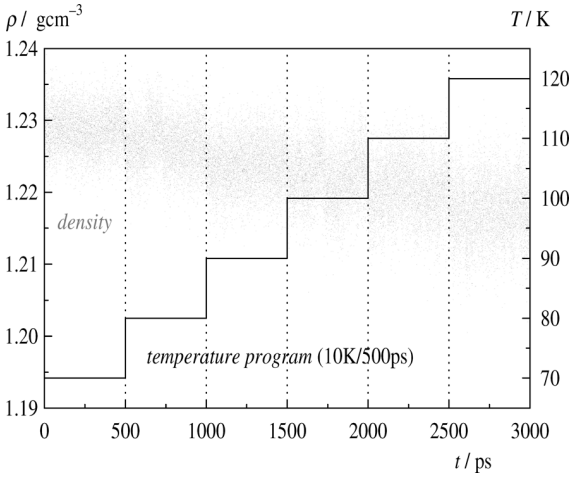

Fig. 3. Development of the density in the NPT ensemble using the COMPASS force field (grey) subjected to the shown temperature program (black) at 0.3 GPa.

respectively, for the unperturbed values and the potential function parameters of the CVFF force field [63], i.e., $k_l = 22.62$ kJ nm^{-2} and $k_\theta = 209.2$ kJ deg^{-2}. In both cases the geometry of a fully relaxed configuration obtained by use of COMPASS (i.e. the last frame at 70 K) was used for initialization, followed by a 1.5 ns NPT run at 70 K to allow the system to rearrange due to the new parameters, which is especially important for the SPC/E* system, where already intramolecular parameters (bond length and angle) largely differ from those of COMPASS.

3. Results and discussion

In Fig. 4 dilatometric simulation curves, i.e., density versus temperature profiles for several heating/cooling cycles are shown. Starting from u-HDA (prepared as stated above) the density first slightly decreases with increasing temperature, then remains nearly constant up to $T = 160$ K and then continuously increases upon *cooling*. Thus, in total the density increases from 1.149 g cm^{-3} to 1.170 g cm^{-3} at 70 K in the first cycle. In the second cycle at low temperatures the same densities are obtained during heating as previously found during cooling. However, at higher temperatures the density increases again to ca. 1.187 g cm^{-3} at $T = 200$ K and further to ca. 1.225 g cm^{-3} when cooling to 70 K. In the third cycle the data points closely follow the results of the second cooling process during heating (up to 220 K) as well as during cooling to the initial temperature of 70 K. Obviously, in the first and second cycle irreversible relaxation occurred yielding more compact structures, while the results of the

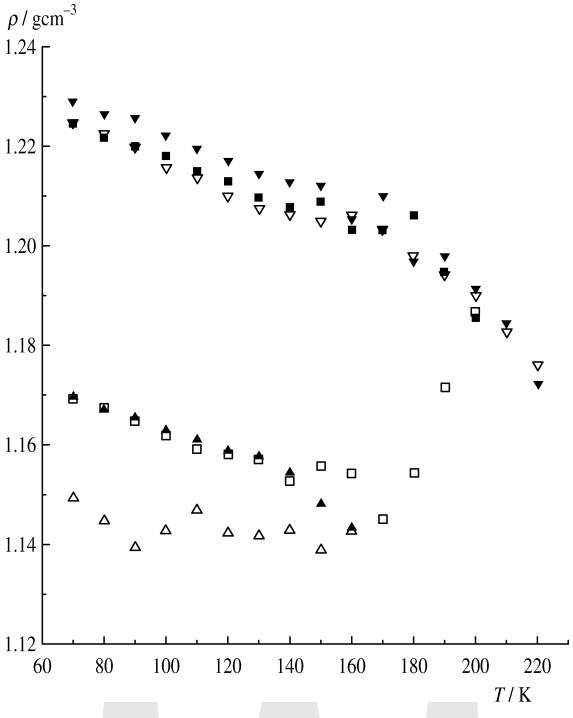

Fig. 4. Density versus temperature for the first (triangles), second (squares) and third (inverted triangles) cycle using the COMPASS force field with open symbols for heating and full symbols for cooling runs.

third cycle are characteristic of a system in equilibrium with a reversible behavior upon heating and cooling. Thus, the third heating/cooling cycle (and subsequent cycles) can be employed to search for the glass-to-liquid transition, while the irreversible structural relaxation seen in the first two cycles hide a possible glass-to-liquid transition.

In Fig. 5 two further independent heating runs (both starting from the last configuration of the third cooling process) are shown together with the results of the third cooling depicted as error bars (the height of it being double the standard deviation of individual data points). Apart from 180 K, data points are located within the error bars of the previous run confirming the reversible and reproducible behavior. Close inspection of the diagram reveals three regions: a narrow one around 170 K with relatively large fluctuations and two regions above and below with linear dependence of density on temperature. The slope at low temperature reads as (0.02 g cm^{-3}) / (100 K) while at high temperatures the slope amounts to an appreciably larger value of (0.03 g cm^{-3}) / (30 K). The change in slope may be interpreted as a transition from glassy HDA (at $T <$ 155 K) to a highly viscous liquid HDL (at $T >$ 185 K). As fluctuations are

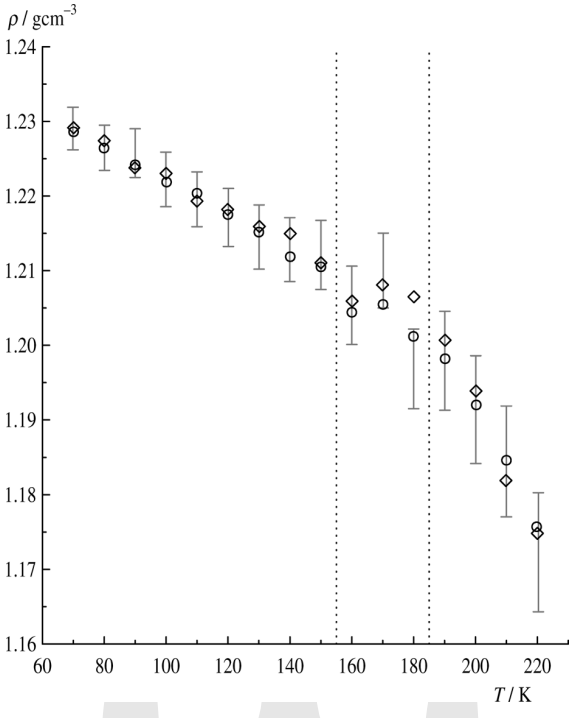

Fig. 5. Density versus temperature for two independent heating runs indicated by circles and diamonds, respectively, using the COMPASS force field. In addition, the results of the previous cooling run are given in form of (grey) error bars (height = double standard deviation). The region between the vertical lines (dotted) is interpreted as the glass transition range.

largest close to T_g, the fluctuating behavior in the middle region corroborates the existence of a glass transition with a width of about 30 K at the heating/cooling rates employed in the simulation. We, therefore, extract $T_g \approx 170 \pm 15$ K for the model system under consideration from the data in Fig. 5.

In Fig. 6 preliminary results are shown for the SPC/E* and TIP3P* system. Omitting the previous relaxation run, error bars are shown for the first cooling and data points for the second heating cycle. Qualitatively, the results are quite similar to those obtained with COMPASS, although densities are larger and the glass transition area seems to be shifted to higher temperatures. Rather crudely the glass-transition range could be estimated to 175–245 K for SPC/E* and 165–215 K for TIP3P*. However, further investigations are necessary to corroborate these results.

In addition to the $\rho(T)$ plot, T_g may be also derived from a change in the mobility, e.g., characterized by the diffusion coefficient D. D may be extracted from the limiting slope from a plot of the mean square displacement (*msd*) of

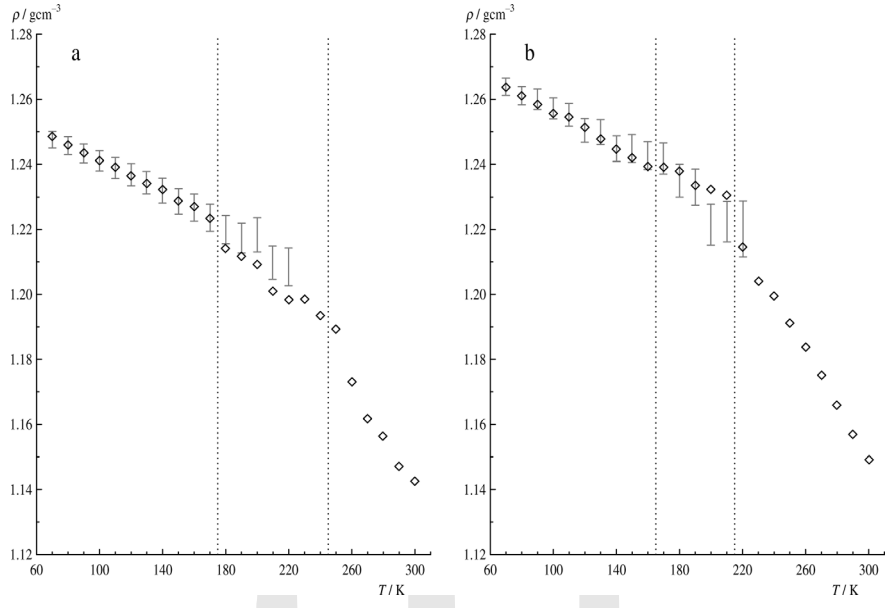

Fig. 6. Density versus temperature for the second heating run using force fields SPC/E* (a) and TIP3P* (b). In addition, the results of the first cooling run are given in form of (grey) error bars (height = double standard deviation). The region between the vertical lines (dotted) is interpreted as the glass transition range.

the center of gravity of the molecules (or more simply from the mean square displacement of oxygen atoms) versus time,

$$D = \frac{1}{6}\lim_{t\to\infty}\frac{\mathrm{d}\,msd}{\mathrm{d}t}$$

where

$$msd = \left\langle \left|\mathbf{r}_i(t) - \mathbf{r}_i(0)\right|^2 \right\rangle$$

and $r_i(t)$ is the position of the i^{th} oxygen atom at a particular time [64]. However, the NPT trajectories discussed above are not suitable because of the type of thermostat (Andersen) chosen, which disturbs the trajectory in a stochastic way. Thus, for each temperature starting from a representative frame (with respect to actual density and pressure) taken from the last heating cycle, a 200 ps NVE run was performed. Alternatively NVT runs with the Nosé [65] instead of the Andersen thermostat could be performed; however, temperature as well as pressure are fairly well retained within the short NVE runs executed. From these 200 ps runs the first 25 ps are discarded to overcome the influence of the input NPT data and D is evaluated from the slope of *msd* data points belonging to the range 50–150 ps. Still larger times are not used because these final time points are showing rather poor statistics. After reinitialization of the velocities of the start-

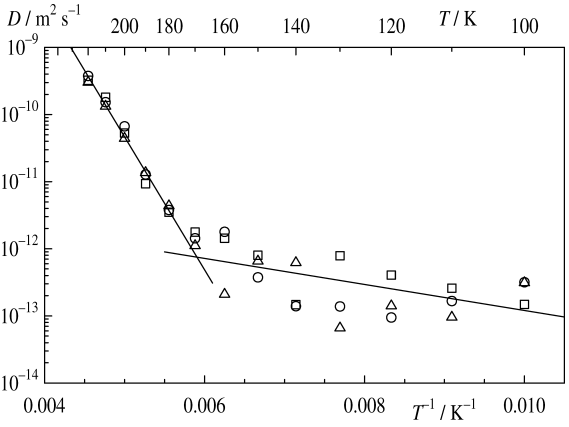

Fig. 7. Arrhenius-like plot of the self diffusion coefficient D, i.e., $\log(D)$ versus reciprocal temperature. Symbols refer to three independent NVE runs. Straight lines are obtained from linear regression of data points belonging to temperatures smaller or larger 170 K, respectively, and intersect at $T \approx 169$ K.

ing systems according to the actual temperature the whole procedure was repeated twice in order to obtain three independent estimates for D at each temperature. In a linear D versus T plot D values are on the order of $(10^{-13}$–$10^{-12})$ m^2s^{-1} up to $T \approx 180$ K and then rapidly increase to $3.5\ 10^{-10}$ m^2s^{-1} at $T = 220$ K. The value at the high temperature end is in good accordance with TIP4P-Ew water [66] (ca. $3\ 10^{-10}$ m^2s^{-1} at 230 K) and slightly larger than the experimental value reading as ca. $0.8\ 10^{-10}$ m^2s^{-1} at $T = 220$ K and 0.3 GPa [67, 68]. In Fig. 7 the data are depicted in a semi-logarithmic plot against $1/T$ (although the temperature dependence of the diffusion coefficient of water is known to deviate from Arrhenius behavior). Nevertheless, data points are fairly well located on a straight line for temperatures above 180 K, while in the range of low temperatures D is showing largely scattering data with a rather small dependence on T (or $1/T$). Intersection of the two lines both resulting from linear regression of respective data points occurs at 0.0059 K^{-1} corresponding to $T \approx 169$ K in accordance with the glass transition range obtained via "dilatometric" simulation.

In Fig. 8 the enthalpy H (calculated from the simulations as the sum of potential energy, kinetic energy and $p\langle V \rangle$ in kJ per mol water) is plotted as a function of temperature. At temperatures above $T \approx 170$ K the data points clearly deviate from linearity, which is again indicative of the glass-to-liquid transition. As a guide to the eye two straight lines (obtained by linear regression of data points below and above 170 K) intersecting at $T \approx 174$ K are shown, which fit to the glassy state data points at temperatures below the intersection point and to the liquid state data points at temperatures above. The first derivative of the $H(T)$-plot in Fig. 8 yields the $c_p(T)$-plot typically obtained in DSC experiments

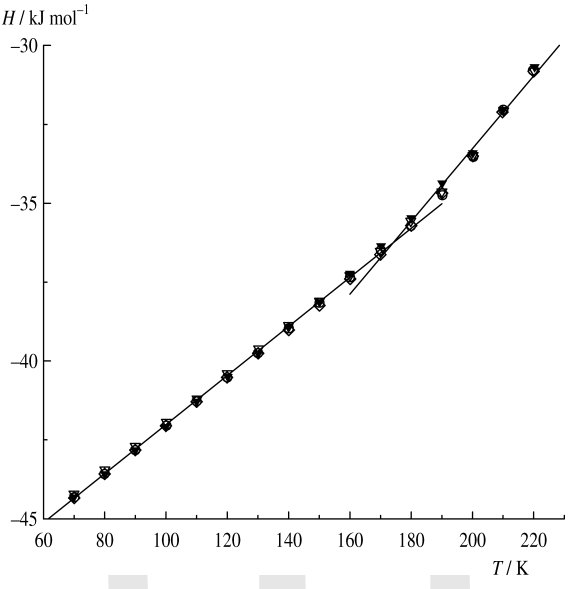

Fig. 8. Enthalpy H versus temperature T. Symbols as in Fig. 4 and Fig. 5. Straight lines are obtained from linear regression of data points belonging to temperatures smaller or larger 170 K, respectively, and intersect at $T \approx 174$ K.

and shows the stepwise increase in $c_p(T)$ at T_g. Thus, three independent methods locate the glass-to-liquid transition at 169–174 K, with a glass-transition width of ≈30 K.

It remains to compare the structure of the model system with data of experimentally obtained HDA. In Fig. 9 calculated X-ray diffractograms (Cu-Kα, 1.54 Å) of the unrelaxed initial configuration and of an equilibrium configuration at the end of the third cooling run are shown together with experimentally obtained diffractograms of unrelaxed u-HDA (prepared by pressure induced amorphization of ice I at 77 K [69]) and structurally relaxed, expanded-HDA (e-HDA, prepared by heating u-HDA twice to 136 K at 0.2 GPa) [3, 51, 70, 71]. In both cases the correspondence is good. Please note that the sharp reflexes in the experimental powder diffractograms at ≈44° result from the sample carrier and the sharp reflexes at ≈22°, 24° and 26° in case of e-HDA arise from traces of hexagonal ice [70]. Similarly, O–O and O–H radial distribution functions of simulated and experimentally obtained u-HDA correspond fairly well, as may be seen from Fig. 10. In this figure the number of oxygen or hydrogen neighbors, respectively,

$$N(r) = \int_0^r \rho(r) \cdot 4\pi r^2 \mathrm{d}r = \int_0^r g(r) \cdot \overline{\rho} \cdot 4\pi r^2 \mathrm{d}r$$

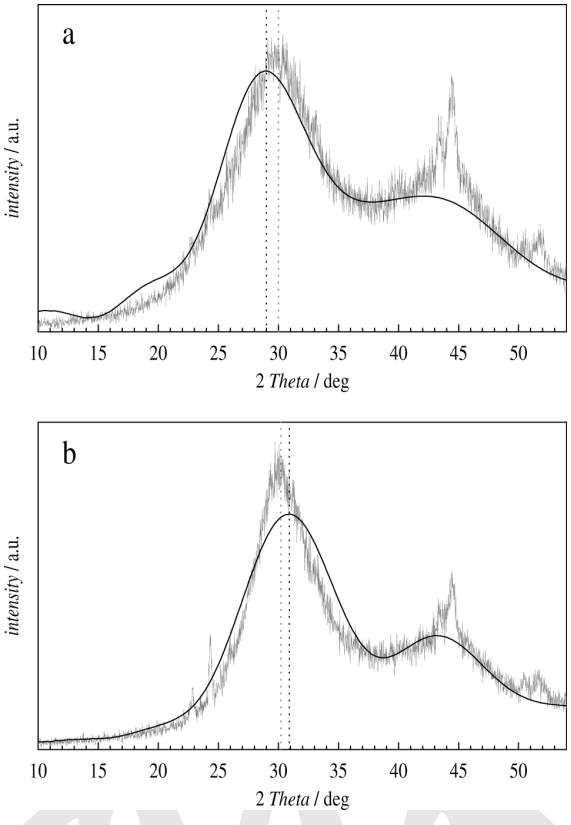

Fig. 9. Diffractograms of simulated (black) and experimental (grey) u-HDA prepared by pressure-induced amorphization of hexagonal ice at 77 K (a) and e-HDA prepared by isobarically heating u-HDA twice to 136 K at 0.2 GPa (b). Dotted vertical lines indicate the position of the first halo peak.

within a distance r is shown as well ($\rho(r)$ and $\overline{\rho}$ being the distance dependent and average density of oxygen or hydrogen, respectively). Integration over the range of the first peak yields the coordination number of the first coordination sphere, reading ca. 4.7 for oxygen and ca. 2.0 for hydrogen. Analogously, values 5.2 (oxygen) and again 2.0 (hydrogen) are obtained for relaxed e-HDA, the latter value in both cases being expected due to the number of covalent bonds. 4.7 and 5.2 closely correspond to a coordination number 5, experimentally found for HDA [15, 72].

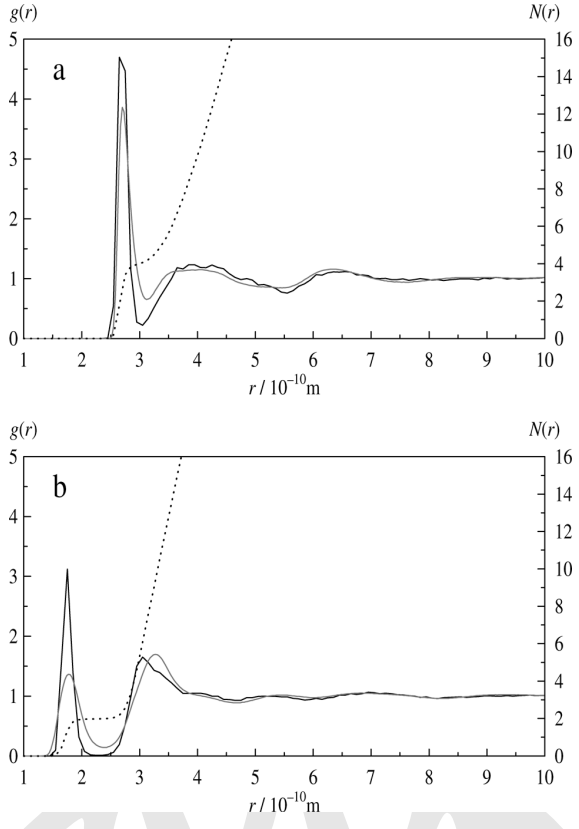

Fig. 10. Radial distribution function $g(r)$ (full line) and number of neighbors $N(r)$ (dotted line) for simulated (black) and experimental (grey) u-HDA for O–O pairs (a) and O–H pairs (b).

4. Conclusions

In conclusion, we have employed molecular dynamics simulations using the COMPASS force field to search for the glass-to-liquid transition in high density amorphous ice (HDA). We have used three different methods of locating the glass-to-liquid transition temperature T_g at a pressure $p \approx 0.3$ GPa, namely (i) the observation of a deviation from linear $\rho(T)$ behavior in the temperature range $T_g \approx 170\pm15$ K in Fig. 5, (ii) a rapid increase of the diffusion coefficient D at $T_g \approx 169$ K in Fig. 7, and (iii) a deviation from linearity in an $H(T)$ plot at $T_g \approx 174$ K in Fig. 8. In addition, powder X-ray diffractograms generated from the atomistic structure of the model system compare favorably with our own experimental powder X-ray diffractograms as shown in Fig. 9. Also the radial distribution functions (RDFs) determined from neutron diffraction experiments and EPSR refinement [15, 72] fit the model system RDFs well (cf. Fig. 10).

Even though the temperatures obtained from simulations typically deviate significantly from experimental temperatures, our simulations suggest that HDA may indeed be a proxy to an ultraviscous high density liquid (HDL) at low temperatures.

Acknowledgement

We are grateful to Nicolas Giovambattista and Francis W. Starr for discussing our findings and funding from the European Research Council (Starting Grant SULIWA) and the Austrian Science Fund FWF (START Award Y391).

References

1. P. G. Debenedetti, J. Phys.: Condens. Matter **15** (2003) R1669.
2. C. A. Angell, Annu. Rev. Phys. Chem. **55** (2004) 559.
3. T. Loerting, N. Giovambattista, J. Phys. Cond. Matt. **18** (2006) R919.
4. C. Lobban, J. L. Finney, W. F. Kuhs, Nature **391** (1998) 268.
5. C. G. Salzmann, P. G. Radaelli, A. Hallbrucker, E. Mayer, J. L. Finney, Science **311** (2006) 1758.
6. O. Mishima, H. E. Stanley, Nature **396** (1998) 329.
7. E. F. Burton, W. F. Oliver, Proc. R. Soc. Ser. A **153** (1935) 166.
8. P. Brüggeller, E. Mayer, Nature **288** (1980) 569.
9. J. Lepault, R. Freeman, J. Dubochet, J. Microscopy **132** (1983) RP3.
10. O. Mishima, L. D. Calvert, E. Whalley, Nature **310** (1984) 393.
11. E. Mayer, J. Appl. Phys. **58** (1985) 663.
12. T. Loerting, C. Salzmann, I. Kohl, E. Mayer, A. Hallbrucker, Phys. Chem. Chem. Phys. **3** (2001) 5355.
13. G. Strazzulla, G. A. Baratta, M. E. Palumbo, Spectrochim. Acta **57A** (2001) 825.
14. T. Loerting, W. Schustereder, K. Winkel, C. G. Salzmann, I. Kohl, E. Mayer, Phys. Rev. Lett. **96** (2006) 025702.
15. D. T. Bowron, J. L. Finney, A. Hallbrucker, I. Kohl, T. Loerting, E. Mayer, A. K. Soper, J. Chem. Phys. **125** (2006) 194502.
16. G. P. Johari, A. Hallbrucker, E. Mayer, Nature **330** (1987) 552.
17. C. A. Angell, J. Phys. Cond. Matter **19** (2007) 205112.
18. O. Andersson, Phys Rev. Lett. **95** (2005) 205503.
19. O. Andersson, A. Inaba, Phys. Rev. B **74** (2006) 184201.
20. O. Mishima, Y. Suzuki, J. Chem. Phys. **115** (2001) 4199.
21. J. S. Tse, J. Chem. Phys. **96** (1992) 5482.
22. O. Mishima, Nature **384** (1996) 546.
23. J. S. Tse, D. D. Klug, C. A. Tulk, I. Swainson, E. C. Svensson, C. K. Loong, V. Shpakov, V. R. Belosludov, R. V. Belosludov, Y. Kawazoe, Nature **400** (1999) 647.
24. F. H. Stillinger, A. Rahman, J. Chem. Phys. **60** (1974) 1545.
25. P. H. Poole, F. Sciortino, U. Essmann, H. E. Stanley, Nature **360** (1992) 324.
26. P. H. Poole, U. Essmann, F. Sciortino, H. E. Stanley, Phys. Rev. E **48** (1993) 4605.
27. U. Essmann, A. Geiger, J. Chem. Phys. **103** (1995) 4678.
28. C. J. Roberts, P. G. Debenedetti, F. H. Stillinger, J. Phys. Chem. B **103** (1999) 10258.
29. F. W. Starr, M.-C. Bellissent-Funel, H. E. Stanley, Phys. Rev. E **60** (1999) 1084.
30. N. Giovambattista, H. E. Stanley, F. Sciortino, Phys. Rev. Lett. **91** (2003) 115504.
31. N. Giovambattista, H. E. Stanley, F. Sciortino, Phys. Rev. E **72** (2005) 031510.

32. C. Vega, C. McBride, E. Sanz, J. L. F. Abascal, Phys. Chem. Chem. Phys. **7** (2005) 1450.
33. H. E. Stanley, C. A. Angell, U. Essmann, M. Hemmati, P. H. Poole, F. Sciortino, Physica A **205** (1994) 122.
34. C. J. Roberts, G. A. Karayiannakis, P. G. Debenedetti, Ind. & Eng. Chemi. Res. **37** (1998) 3012.
35. G. Franzese, G. Malescio, A. Skibinsky, S. V. Buldyrev, H. E. Stanley, Nature **409** (2001) 692.
36. S. V. Buldyrev, H. E. Stanley, Physica A **330** (2003) 124.
37. I. Brovchenko, A. Geiger, A. Oleinikova, J. Chem. Phys. **118** (2003) 9473.
38. R. Martonak, D. Donadio, M. Parrinello, Phys. Rev. Lett. **92** (2004) 225702.
39. R. Martonak, D. Donadio, M. Parrinello, J. Chem. Phys. **122** (2005) 134501.
40. I. Brovchenko, A. Geiger, A. Oleinikova, J. Chem. Phys. **123** (2005) 044515.
41. N. Giovambattista, H. E. Stanley, F. Sciortino, Phys. Rev. Lett. **94** (2005) 107803.
42. L. Xu, P. Kumar, S. V. Buldyrev, S.-H. Chen, P. H. Poole, F. Sciortino, H. E. Stanley, PNAS **102** (2005) 16558.
43. P. H. Poole, I. Saika-Voivod, F. Sciortino, J. Phys.: Cond. Matter **17** (2005) L431.
44. J. Zarzycki, *Glasses and the vitreous state*. Cambridge University Press, Cambridge, UK (1991).
45. M. S. Elsaesser, I. Kohl, E. Mayer, T. Loerting, J. Phys. Chem. B **111** (2007) 8038.
46. K. G. Wagner, M. Maus, A. Kornherr, G. Zifferer, Chem. Phys. Lett. **406** (2005) 90.
47. M. Maus, K. G. Wagner, A. Kornherr, G. Zifferer, Mol. Simul. **34** (2008) 1197.
48. A. Simperler, A. Kornherr, R. Chopra, P. A. Bonnet, W. Jones, W. D. S. Motherwell, G. Zifferer, J. Phys. Chem. B **110** (2006) 19678.
49. N. Giovambattista, C. A. Angell, F. Sciortino, H. E. Stanley, Phys Rev. Lett. **93** (2004) 047801.
50. J. Liu, S.-Y. Wang, C.-P. Zheng, L.-J. Xin, D. Wang, M.-H. Sun, Chin. Phys. Lett. **24** (2007) 2025.
51. R. J. Nelmes, J. S. Loveday, T. Straessle, C. L. Bull, M. Guthrie, G. Hamel, S. Klotz, Nature Physics **2** (2006) 414.
52. H. C. Andersen, J. Chem. Phys. **72** (1980) 2384.
53. L. Verlet, Phys. Rev. **159** (1967) 98.
54. M. J. Hwang, T. P. Stockfisch, A. T. Hagler, J. Am. Chem. Soc. **116** (1994) 2515.
55. H. Sun, Macromolecules **28** (1995) 701.
56. H. Sun, J. Phys. Chem. B **102** (1998) 7338.
57. H. Sun, P. Ren, J. R. Fried, Comput. Theor. Polym. Sci. **8** (1998) 363.
58. H. Sun, P. Ren, J. R. Fried, Comput. Theor. Polym. Sci. **8** (1998) 229.
59. S. W. Bunte, H. Sun, J. Phys. Chem. B **104** (2000) 2477.
60. D. Rigby, Fluid Phase Equilib. **217** (2004) 77.
61. W. L. Jorgensen, J. Chandrasekhar, J. D. Madura, R. W. Impey, M. L. Klein, J. Chem. Phys. **79** (1983) 926.
62. H. J. C. Berendsen, J. R. Grigera, T. P. Straatsma, J. Phys. Chem. **91** (1987) 6269.
63. P. Dauber-Osguthorpe, V. A. Roberts, D. J. Osguthorpe, J. Wolff, M. Genest, A. T. Hagler, Proteins: Struct., Funct., Genet. **4** (1988) 31.
64. A. Simperler, A. Kornherr, R. Chopra, W. Jones, W. D. S. Motherwell, G. Zifferer, Carbohydr. Res. **342** (2007) 1470.
65. S. Nose, Mol. Phys. **52** (1984) 255.
66. J. Holzmann, R. Ludwig, A. Geiger, D. Paschek, Angew. Chem., Int. Ed. **46** (2007) 8907.
67. F. X. Prielmeier, E. W. Lang, R. J. Speedy, H. D. Ludemann, Phys. Rev. Lett. **59** (1987) 1128.
68. F. X. Prielmeier, E. W. Lang, R. J. Speedy, H. D. Luedemann, Ber. Bunsen-Ges. Phys. Chem. **92** (1988) 1111.

69. O. Mishima, L. D. Calvert, E. Whalley, J. Phys. Colloq. **C8** (1984) 239.
70. K. Winkel, M. S. Elsaesser, E. Mayer, T. Loerting, J. Chem. Phys. **128** (2008) 044510.
71. K. Winkel, M. S. Elsaesser, M. Seidl, M. Bauer, E. Mayer, T. Loerting, J. Phys. Cond. Matt. **20** (2008) 494212.
72. J. L. Finney, A. Hallbrucker, I. Kohl, A. K. Soper, D. T. Bowron, Phys. Rev. Lett. **88** (2002) 225503.